Dual Injection in a CO_2 Microwave Plasma: Exploring Post-Plasma Quenching with CH_4 and Comparison with DRM

E.R. Mercer[1,2], M. Albrecht[1,2], R. De Meyer[1,2,3,4], I. Fedirchyk[1,2], E. Morais[1,2], S. Bals[3,4], A. Bogaerts[1,2].

[1]Research group PLASMANT, Department of Chemistry, University of Antwerp, Belgium
[2]Electrification Institute, University of Antwerp, Belgium
[3]Research group EMAT, Department of Physics, University of Antwerp, Belgium
[4]NANOlight Center of Excellence, University of Antwerp, Belgium

Corresponding Author: Elizabeth.Mercer@UAntwerpen.be

Supporting Information

S.1 Liquid Analysis

The liquid samples collected from the post-plasma condenser during dual injection experiments were characterized using multiple analytical techniques to identify and quantify various components. Each set of data was defined by a single CO_2:CH_4 ratio, meaning for both power conditions and all pressure sets, a single liquid sample was collected (e.g., 1 sample = 1:1 CO_2:CH_4, 7:7 slm; but with power being either 1000 or 1250 W, and pressure between 200 – 900 mbar). This approach was chosen to limit the number of samples requiring external analysis and because the experimental setup was not designed to collect individual liquid samples for each condition while in operation.

Since this study represents the first approach to investigating dual injection in a CO_2 MW plasma as a method to utilize reactive quenching, the experimental design prioritized capturing overall trends rather than optimizing sample collection for every parameter combination. As such, certain limitations in data resolution were unavoidable. However, the results provide a foundational understanding of the process, highlighting key trends that will inform future studies where more refined collection strategies can be implemented.

The liquid samples were analyzed using an Interscience Focus GC equipped with a flame ionization detector (FID). Analysis was performed using a Stabilwax column (30 m × 0.32 mm ID, 1.00 μm film thickness) with split injection through the split/splitline (S/SL) injector. Despite comprehensive analysis, no significant volatile compounds were detected using this method.

High performance liquid chromatography (HPLC) analysis was performed using a Waters Alliance e2695 system equipped with both photodiode array (PDA) and refractive index (RI) detectors. Separation was achieved using a Shodex RSpak KC-811 column (6 μm particle size, 8.0 × 300 mm), which is specifically designed for organic acid analysis. The mobile phase consisted of 10 mM H_2SO_4 run under isocratic conditions. This analysis successfully identified and quantified formaldehyde, formic acid, and acetic acid in the liquid samples.

Total organic carbon (TOC) was measured using a Shimadzu TOC-L analyzer. Samples were appropriately diluted prior to analysis to ensure measurements fell within the calibration range of the instrument. The results from this analysis provided the total carbon content of the liquid

samples, which was compared with the sum of carbon-containing compounds identified by the HPLC analysis to assess the completeness of compound identification. Only a small difference was found, and can be seen in *Figure 10A*, in the main text.

Gas chromatography-mass spectrometry (GC-MS) analysis was conducted using an Interscience GC 8000 Top system coupled to a mass spectrometer. The separation was performed on an Agilent DB-5MS UI column (30 m × 0.320 mm, 0.25 μm film thickness). This technique did not yield significant additional information about the composition of the liquid samples.

Liquid chromatography-mass spectrometry (LC-MS) analysis was performed using a Waters Acquity Arc system. Separation was conducted on a CORTECS C18 Column (90Å, 2.7 μm particle size, 4.6 mm × 50 mm), which is a general-purpose reverse-phase column. A gradient elution method was employed with the following mobile phase composition:

Table S.1 | Mapping of the gradient elution employed in LC-MS analysis.

Time (min)	Water (%)	Acetonitrile (ACN%)
Initial	95	5
0.5	95	5
8.0	5	95
8.5	5	95
10	95	5

The flow rate was maintained at 1.2 mL/min. This analysis revealed the presence of an unidentified compound with a molecular weight of 180 g/mol, which was not detected by other analytical methods.

UV-Visible spectroscopy (UV-Vis, Shimadzu UV-2600i) equipped with a deuterium lamp, a tungsten halogen lamp, and a photomultiplier detector, was used to characterize the chromophoric properties of the liquid samples. This analysis helped identify the absorption maxima and provided insights into the presence of conjugated systems within the unidentified compounds in the liquid products.

S.1.2 Carbon Analysis

After each of the experimental runs, carbon was collected from the bellows and cyclone separator. A set of data is again defined by a single $CO_2:CH_4$ ratio, meaning for both power conditions and all pressure sets, a single sample was collected (e.g., 1 sample = 1:1 $CO_2:CH_4$, 7:7 slm; and either 1000 or 1250 W, and one pressure in the range of 200 – 900 mbar, although no carbon formation was observed at $p < 700$ mbar), for the same reason as explained for the liquid analysis.

A small amount of dark carbonaceous deposits was also found on the reactor walls and in the KF piece downstream of the quartz tube, with only very few deposits found in the cyclone separator. All deposits were collected using a paper tissue for subsequent characterization. The different samples were characterized via scanning electron microscopy (SEM) and transmission electron microscopy (TEM). A portion of the collected material was suspended in acetone (for SEM) or chloroform (for TEM) and dispersed by sonication.

For SEM analysis, a few drops of the suspension were deposited onto an aluminum stub and left to dry before being placed in the SEM for characterization. For TEM analysis, a holey carbon TEM grid was positioned on filter paper, and a few drops of the suspension were applied to the grid and allowed to dry. After a brief drying period, the grid was ready for TEM analysis.

The deposited carbon is analyzed using two methods, Scanning Electron Microscopy (SEM), executed using a ThermoFisher Scientific Quanta FEG 250 operating at 20 kV in high vacuum mode, and Transmission Electron Microscopy (TEM) performed using a ThermoFisher Scientific Tecnai Osiris G20 operating at 200 kV, with images acquired in bright-field TEM (BF-TEM) mode [1].

S.1.3 Optical Emission Spectroscopy Data Treatment

Optical emission spectroscopy (OES) measurements were performed to characterize the plasma emission. The acquired spectral data (200 – 800 nm) underwent a comprehensive treatment process to ensure accurate quantitative analysis. Spectral measurements were obtained within the resonance chamber of the reactor to determine plasma composition.

Spectra were acquired using an Ocean Insight mini spectrometer (HR-4UVV250-5) equipped with a solarization-resistant fiber with a diameter of 400 μm (QP400-2-SR) and cosine corrector with Spectralon diffusing material (CC-3-UV-S). For each experimental condition (varying power, pressure, and flow rates), single-shot spectra were collected along with an electronic dark measurement.

The raw spectral intensities were calibrated using a standard irradiance calibration to convert arbitrary intensity counts to absolute radiometric units (μJ/count), accounting for the spectrometer's wavelength-dependent response. The collection geometry was calculated accounting for the cosine corrector properties, with a diffuser diameter of 3900 μm. For the cosine corrector following Lambert's law, the radiance was integrated over a hemisphere (2π steradians). The calibrated energy values were then converted to photon flux (photons/s/m²). An adaptive Savitzky-Golay filter was applied to the photon flux data with parameters optimized for spectroscopic data (window length = 15, polynomial order = 5). Different smoothing parameters were applied to baseline and peak regions to preserve spectral features while reducing noise. Finally, the spectra were normalized by their maximum intensity values for comparative analysis across different experimental conditions. An example spectrum is presented in *Figure S.1*.
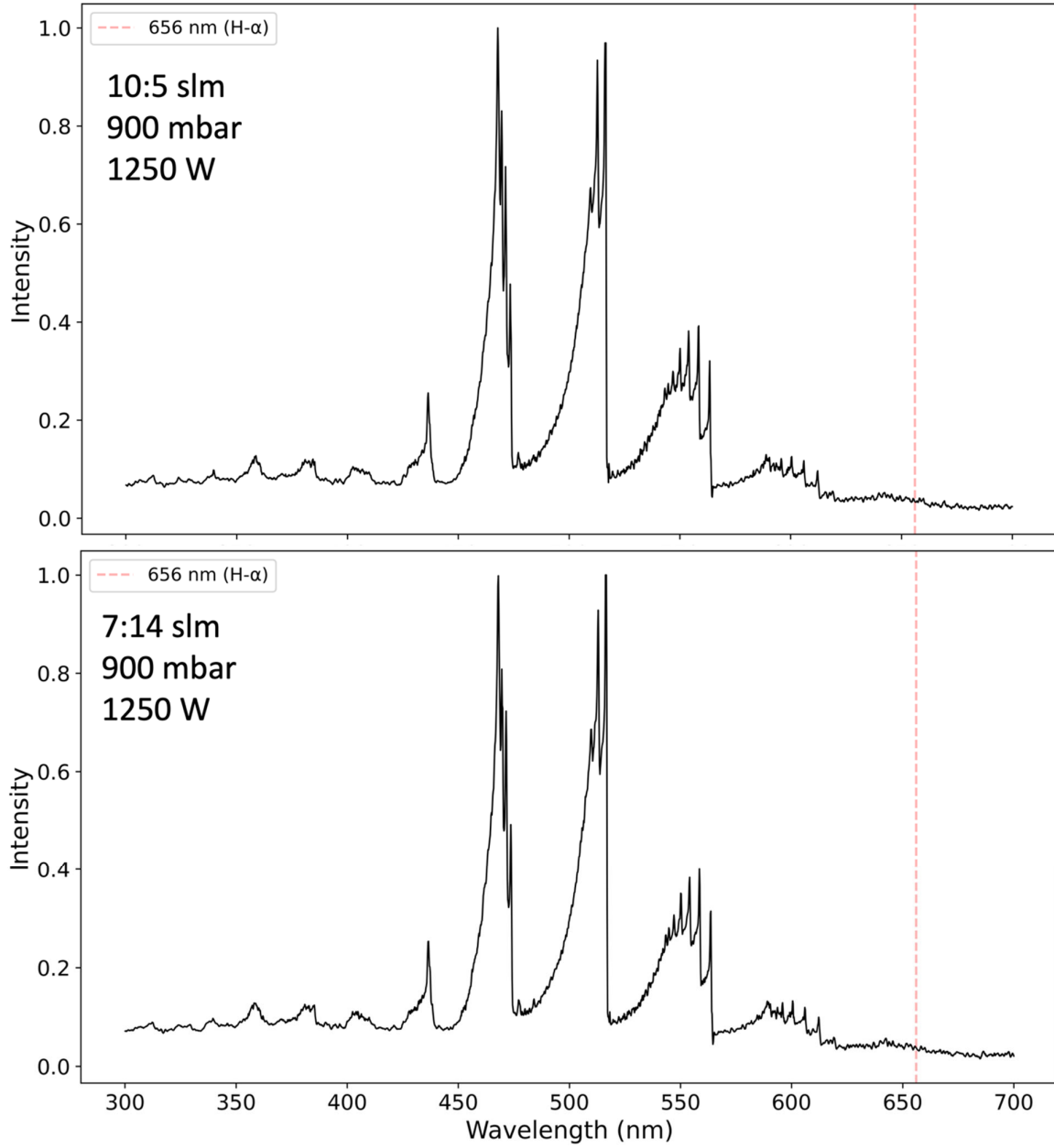
Figure S.1 | Example of treated spectrum of C₂ ($d^3\Pi_g - a^3\Pi_u$) Swan band, used in MassiveOES fitting, as well as an indicator for where the H_α at ~656 nm would be present (red dashed line), which was not found to be present in any of the spectra.

The rotational temperatures (T_{rot}) were determined using the C₂ ($d^3\Pi_g - a^3\Pi_u$) Swan band system within the open-source MassiveOES software package by fitting to a simulated spectrum. Here we consider T_{rot} as a reliable proxy for the gas temperature in contracted plasmas [2], which are typically observed at p > 200 mbar [3]. The accuracy of the temperature determination was assessed by analyzing the residuals between experimental and simulated

spectra to ensure the absence of systematic deviations indicative of non-Boltzmann behavior or other spectroscopic artifacts.

The uncertainties in the extracted temperatures arise from several factors, including the statistical uncertainty in the fitting routine, estimated via the covariance matrix of the least-squares optimization, uncertainties in molecular constants and transition probabilities (which are estimated to be below 2%), and fitting convergence verification through residual analysis and multiple initial conditions.
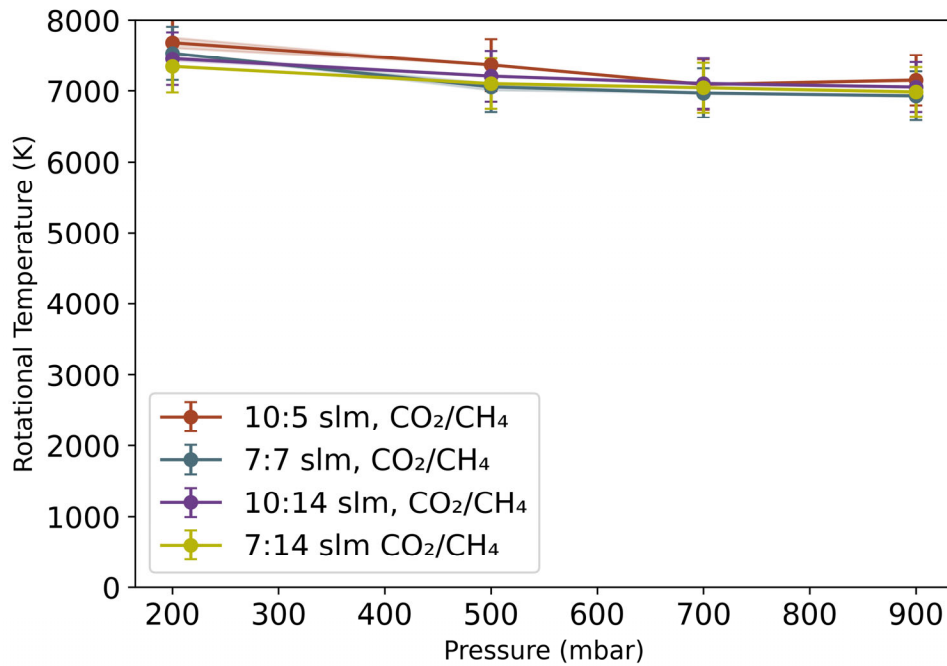
Figure S.2 | Averaged rotational temperature between 1000 and 1250 W, as a function of pressure, for the four different $CO_2:CH_4$ ratios investigated.

All temperatures were found to be between ~7000 – 8000 K, with the lowest pressures (200 mbar) showing somewhat higher temperatures (see *Figure S.2*), consistent with values reported in the literature [2]. The temperatures were consistent across powers, all overlapping within the error bar, as is typically observed in CO_2 plasmas [2, 4, 5]. Therefore, for better visualization, the values were averaged, and presented in *Figure S.2*, with a shaded deviation to show the (small) variability between the two power conditions (1000 and 1250 W), as we do not expect much deviation in the temperature between these power conditions, this provides further

indication of the error in this measurement. The presented error bar is taken as a 5% error of this average, as this data was only used as a starting temperature for the model.

The spectra were used during the experiments to monitor whether CH_4 traveled upstream into the reactive volume, as would be indicated by additional peaks from, for example, H_α at ~656 nm. The treated data indicated that no CH_4 was detectable within the emission spectra, as two examples are shown in *Figure S.1*. These spectra were chosen as they represent the 'extreme' circumstances, where we might see the greatest back flow, if present. We expect to observe the H_α even in small concentrations, as reported by *Kuijpers*, who showed that H_α can be observed in concentrations as low as 0.75% CH_4 [6]. Therefore, the data was used as a single shot temperature measurement taken as the core temperature and utilized as input for the CO_2 plasma temperature in the 0D model, before CH_4 injection, described in *Section S.2*.

S.1.4 Secondary Injection Housing

The secondary, counter-flow injection of CH_4 is applied in the afterglow region, 5 cm from the waveguide, where temperatures exceed 1500 K. A diagram is presented in *Figure S.3*.
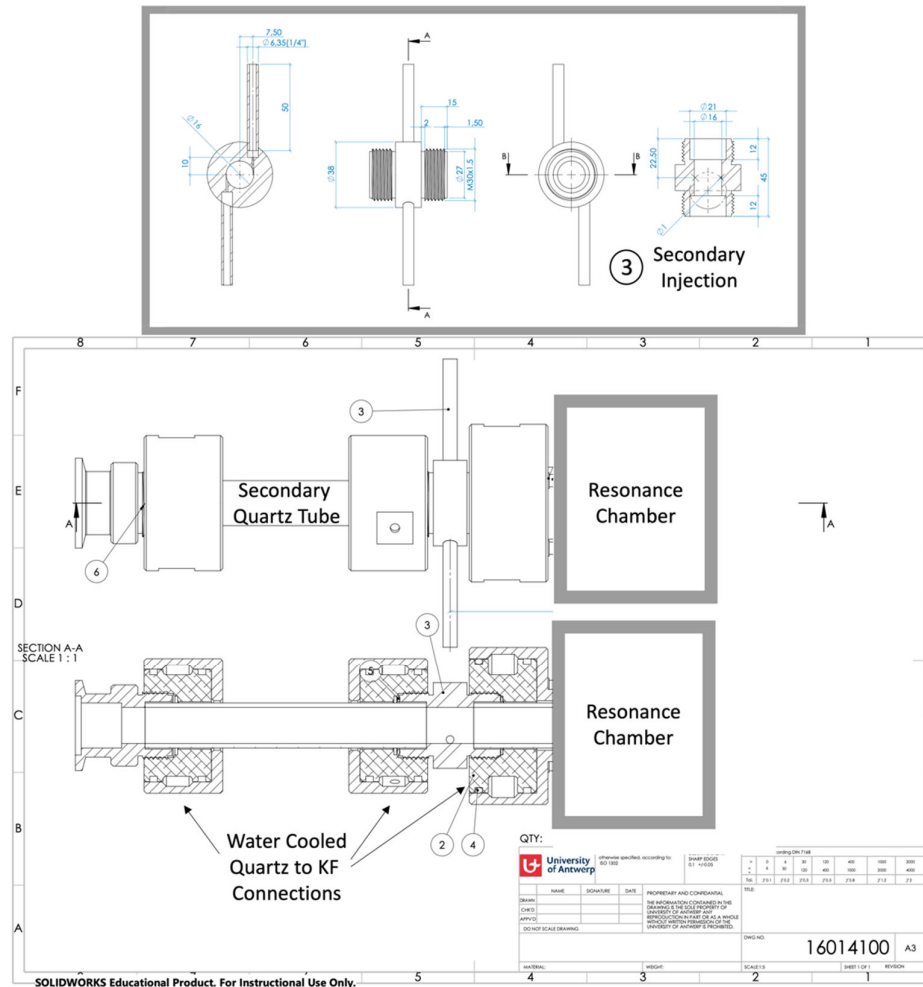

Figure S.3 | Schematic drawing of secondary injection housing with post-plasma viewing with a secondary quartz tube. A detailed view of the secondary tangential injection (3) is at the top of the image.

The secondary counterflow tangential injection was designed to enhance mixing between CH_4 and the post-plasma afterglow region, with two 1 mm inlet nozzles.

S1.5 Gas Chromatography

Gas sampling was conducted using gas chromatography (Agilent 990 MicroGC, two-channel configuration) and an infrared luminescent quenched absorption technique (PyroScience GmbH FDO$_2$ optical oxygen sensor).

The MicroGC system was equipped with two analytical channels:

- **Channel 1**: A Molesieve 5Å column with argon as the carrier gas, used to measure CO, H$_2$, O$_2$, and CH$_4$.
- **Channel 2**: A PoraPLOT U column with helium as the carrier gas, used to measure CO$_2$, C$_2$H$_2$, C$_2$H$_4$, and C$_2$H$_6$.

Both channels included a CP-PoraBond Q precolumn to improve separation. Before entering the columns, the gas mixture was heated to 70°C to ensure consistent analysis conditions. The composition of the post-plasma mixture was determined from the chromatograms. In order to assess the accuracy of the measurements, the 95% confidence interval of each composition determination was calculated according to equations S.E1 - S.E3, taken from [7].

$$S_{x_{sample}} = \frac{S_{y/x}}{b} * \sqrt{\frac{1}{m} + \frac{1}{n} + \frac{(y_{sample} - y_{avg})^2}{b^2 * \sum_i (x_i - x_{avg})^2}} \qquad \text{[S.E1]}$$

$$x_{sample} = \frac{(y_0 - a)}{b} \qquad \text{[S.E2]}$$

$$CI_{95} = x_{sample} \pm t_{(n-2)} * S_{x_{sample}} \qquad \text{[S.E3]}$$

in which the standard deviation ($S_{x_{sample}}$) of each measured component was calculated using the standard deviation of the calibration standards ($\frac{S_{y/x}}{b}$), the slope of the regression line (b), the number of replicas of the measurement (m), the number of calibration standards (n), the response value of the measurement (y_{sample}), the average response of the calibration standards (y_{avg}), the concentration (in %) of standard (x_i), the average concentration (in %) of all standards (x_{avg}). x_{sample} was determined using the intercept ($y_0 - a$) and slope of regression line. The student t-value for a two-tailed distribution at n degrees of freedom ($t_{(n-2)}$) was used to determine the 95% confidence interval. The $S_{x_{sample}}$ was used in calculating the analytical error propagation of the performance metrics reported in this work, see *Section S.1.6*.

S.1.6 Performance Calculations

All calculations for the performance metrics shown in this work follow the methods outlined by *Wanten et al.* [8], to properly account for gas expansion/contraction upon reaction, which is very important to obtain the correct values for the final reported data. We utilized the internal standard method in which nitrogen is mixed downstream before the vacuum pump, as shown in *Figure 1*, in the main text. Therefore, we take both the measured input and output fractions directly so that the flux ratio is equal to the ratio of the obtained fractions of the standard, during the blank (plasma off) and plasma on measurement [8]. The gas expansion coefficient, or flux ratio (α), was calculated using:

$$\alpha = \frac{\dot{n}_{tot}^{out}}{\dot{n}_{tot}^{in}} = \frac{c_{standard}^{in}}{c_{standard}^{out}} = \frac{A_{standard}^{in}}{A_{standard}^{out}} \qquad [S.E4]$$

where the molar flow rate ($\dot{n}$) is assumed constant, with $A_{standard}$ the signal (e.g., peak area on GC) corresponding to the internal standard. The signal and the concentration (c) of the standard are assumed to be linear, and the gas streams are both stable and sufficiently mixed before entering the analytical equipment. $A_{standard}^{in}$ is measured using a blank (or 'plasma off' measurements on the reactants and the internal standard). $A_{standard}^{out}$ is measured during the experimental run, thus giving the relative change in gas expansion or contraction [8].

The absolute conversion (χ_{abs}) is calculated using:

$$\chi_{abs,i} = \frac{y_i^{in} - \alpha \cdot y_i^{out}}{y_i^{in}} \qquad [S.E5]$$

where y_i^{in} is the concentration of the inlet reactant (given by a blank measurement), y_i^{out} is the concentration of the unreacted species at the outlet, as measured by GC. This metric only considers a single reactant. However, when considering the whole input mixture, it is necessary to calculate the effective conversion (χ_{eff}), which is the weighted χ_{abs} with the fraction of the gas at the inlet (y_i^{in}):

$$\chi_{eff} = \chi_{abs} \cdot y_i^{in} \qquad [S.E6]$$

The value for χ_{eff} is used to calculate the total conversion χ_{total}:

$$\chi_{total} = \Sigma_i \chi_{eff_i} \qquad \text{[S.E7]}$$

which takes the sum of the χ_{eff} of each reactant (in our case, CO_2 and CH_4). The value for χ_{total} is used to calculate energy cost (EC):

$$EC_{tot} = \frac{SEI}{\chi_{tot}} \qquad \text{[S.E8]}$$

where SEI is the specific energy input to all reactants (i.e., CO_2 and CH_4) (in kJ/mol, kJ/L, or eV/molecule).

The selectivity for a certain reaction product j is defined as the ratio of the atoms a that are from the conversion of the reactants (i), that result in product (j):

$$S_{j,a} = \frac{\mu_{j,a} * \alpha * c_j^{out}}{\Sigma_i \mu_{i,a} * (c_i^{in} - \alpha * c_i^{out})} \qquad \text{[S.E9]}$$

where $\mu_{j,a}$ is the number of atoms (a) per molecule of j, and $\mu_{i,a}$ is the number of atoms for reactant (i). The measured output concentrations are multiplied with the gas expansion factor, such that the input and output become inflows and outflows instead of concentrations.

For the metrics reported, a standard error propagation analysis was derived using the standard deviation in each of the variables (e.g., concentration, as discussed in *Section S.1.5*, flow rates, and power measurements) to determine the overall uncertainty in each value.

S.2 Modeling

S.2.1 Water-Gas Shift Equilibrium and H₂O Formation

As shown in the main text in *Section 3.1*, the dominant reactions governing CO_2 conversion in our model are:

$$CO_2 + M \leftrightarrows CO + O + M \qquad \text{[SR.1]}$$

$$CO_2 + O \leftrightarrows CO + O_2 \qquad \text{[SR.2]}$$

$$CO_2 + H \leftrightarrows CO + OH \qquad \text{[SR.3]}$$
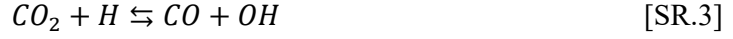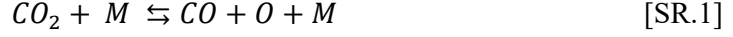
where SR.1 shows the thermal dissociation reaction (which occurs upon collision with a third body, denoted as M), SR.2 represents oxidation by O atoms, also leading to dissociation, and SR.3 is H-mediated conversion. As discussed in the main text, we can assume the chemistry is thermal. The rate coefficients are defined by the GRI-Mech 3.0 reaction mechanism [9], where the reverse rates are calculated according to the principle of detailed balance.

Besides the reduction in back reactions, as explained in *Section 3.1* of the main paper, the addition of CH_4 also leads to a substantial further conversion of CO_2 via SR.3. The reaction of CO_2 with H atoms is related to the reverse water-gas shift reaction, where H_2 reacts with CO_2 to produce CO and H_2O. As CH_4 is oxidized by the available oxygen, the dissociated hydrogen reacts with CO_2, forming CO and H_2O, following the water-gas shift equilibrium:

$$K_{eq}(T) = \frac{[CO_2] \cdot [H_2]}{[CO] \cdot [H_2O]} \qquad \text{[S.E10]}$$

where $K_{eq}(T)$ is the temperature-dependent equilibrium constant of the water-gas shift reaction.

Figure S.4 illustrates the formation of H_2O through the reverse water-gas shift reaction. The solid dark blue line represents the H_2O molar fraction obtained from the kinetic simulation, while the dashed light blue line indicates the H_2O molar fraction calculated from the CO_2, CO, and H_2 concentrations in the model, adhering to the equilibrium defined by $K_{eq}(T)$.
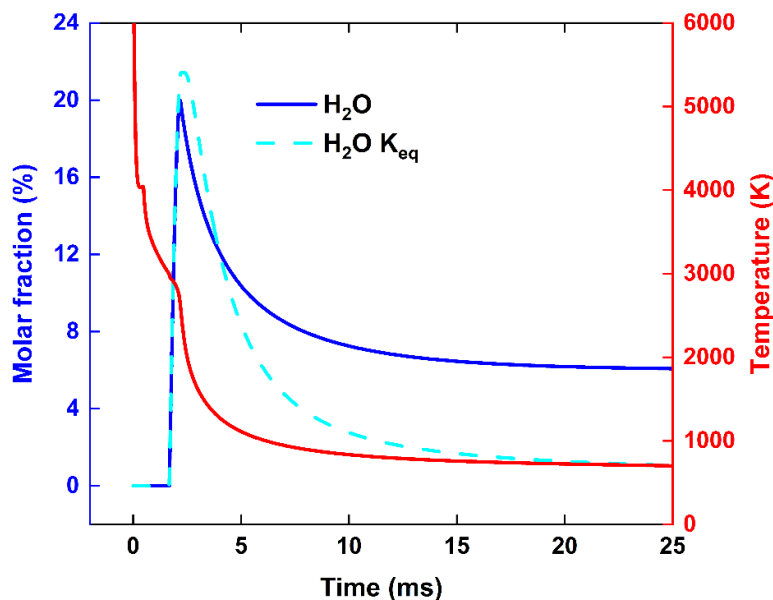
Figure S.4 | H₂O molar fraction as function of time, calculated by the kinetic simulation (solid dark blue line) and predicted by the water-gas shift equilibrium (dashed light blue line), for a pressure of 500 mbar, a power of 1000 W and CO_2:CH_4 ratio of 5:7. The temperature is plotted in red on the right y-axis.

From *Figure S.4*, it is evident that the H_2O concentration initially follows the water-gas shift equilibrium, reaching a maximum H_2O fraction of 20%, corresponding to a gas temperature of approximately 2800 K, which is plotted on the right y-axis. As the simulation proceeds, the H_2O molar fraction diverges from that predicted by the equilibrium, as the temperature is no longer high enough for the reaction kinetics to keep up with the water-gas shift equilibrium. Since $K_{eq}(T)$ decreases with increasing temperature due to the negative Gibbs free energy of the reaction (ΔG_0 = -28.6 kJ/mol), the H_2O fraction predicted by the water-gas shift equilibrium drops below 1 % when the temperature falls below 700 K. In contrast, the H_2O molar fraction predicted by the kinetic simulation stabilizes at a molar fraction of 6%, as the kinetics are too slow to degrade the H_2O This results in a significant amount of H_2O being formed, leading to a relatively low H_2 selectivity of 47%, as shown in *Figure 6* in the main text.

S.2.2 Model Projections for Higher SEI Conditions

Since the addition of CH_4 to the hot CO_2 mixture leads to further CO_2 conversion via the reverse water-gas shift reaction involving the H atoms generated from CH_4 oxidation, the benefit of increased CO_2 conversion is offset by the loss of H_2, leading to low syngas ratios and lower value products formed (H_2O). Additionally, the CH_4 conversion is relatively low, as there is insufficient energy in the CO_2 plasma effluent to achieve efficient CH_4 reforming downstream.

The fact that at these lower SEIs there is low CH_4 conversion and low H_2 selectivity when CH_4 is injected post-plasma was also predicted by the modelling calculations in *Albrechts et al*. [10], and is confirmed experimentally in this study. These modelling calculations show that increasing the SEI would increase the CH_4 conversion and H_2 selectivity, therefore increasing the syngas ratio.

Therefore, we predict that if the plasma input power could be increased while avoiding plasma instability by injecting CH_4 post-plasma, significantly higher syngas ratios can be obtained. This is supported by the model calculations performed in this work, where for a pressure of 900 mbar, SEI of 267 kJ/mol and CO_2: CH_4 ratio of 1:2, absolute CO_2 and CH_4 conversions are obtained of 99.4% and 87.8%, respectively, with a syngas ratio of 1.38, where we assumed a more ideal reactor setup with instant CH_4 injection after the plasma and reduction in wall losses by a factor of 10. Applying an SEI = 240 kJ/mol and CO_2: CH_4 ratio of 1:4 yields absolute CO_2 and CH_4 conversions of 99.7% and 74.6%, with an ideal syngas ratio of 2.06. However, it should be noted that in this scenario, 1200 kJ of heat must be applied per mole of CO_2, likely necessitating a specific and challenging plasma reactor setup.

S.3 Additional Results and Discussion

S.3.1 Additional Analysis
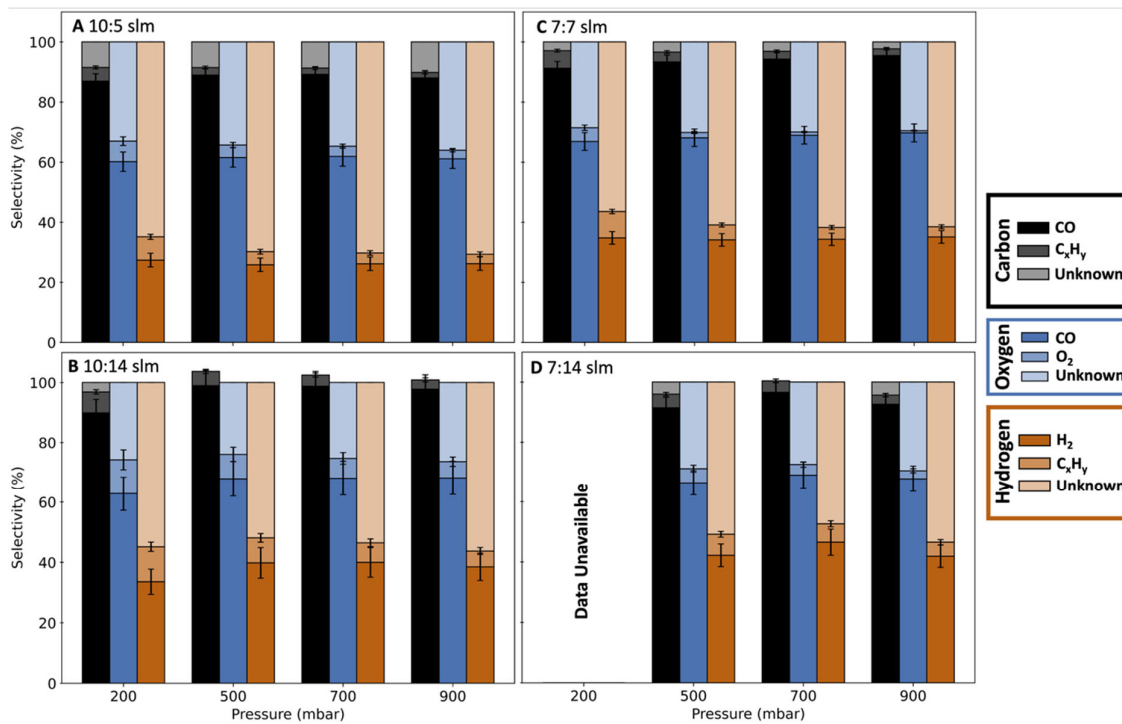
Figure S.5 | Selectivity data as a function of pressure at P = 1000 W for the primary CO₂ flow rate of 10 slm (A and B) and 7 slm (C and D), with different post-plasma injection flow rates of CH₄.

Comparing the 1000 W data of *Figure S.8* with the 1250 W results (*Figure 8*, main text) reveals several important trends. At the lower power input, all configurations maintain high selectivity toward CO formation, though generally 3 – 5% lower than at 1250 W. This reduction is most pronounced for the 1:2 CO_2:CH_4 ratio (*Figure S.5D*), particularly at higher pressures.

The selectivity toward H_2 is consistently lower at 1000 W compared to 1250 W across all conditions, indicating less efficient CH_4 conversion at the lower power input. This aligns with the reduced CH_4 conversion observed at 1000 W (discussed in *Figure 5* and *6* of the main text), suggesting that the reduced thermal energy in the afterglow affects both conversion and product distribution.

The formation of C_2 hydrocarbons (C_2H_2, C_2H_4, and C_2H_6) appears slightly enhanced at 1000 W, particularly evident in the 5:7 and 1:1 CO_2:CH_4 ratio configurations (*Figures S.5B* and *S.5C*). This increased selectivity toward C_2H_x species at lower power suggests that the milder temperature conditions in the afterglow region may favor reaction pathways that produce higher hydrocarbons rather than complete reforming to syngas components.

Similar to the 1250 W data, the "unknown" fractions in C, H, and O balances remain; however, the unknown fraction of C atoms remains low in all conditions presented. Therefore, we conclude that the significant unknown component observed in *Figure S.5* is likely H_2O, as discussed in *Section S.2.2*. The unknown fractions of C likely correspond to carbon (at p > 700 mbar) and the liquid oxygenates (formaldehyde, acetic acid, and formic acid) identified and discussed in *Figure 11* of the main text (at lower pressure), although here the values for unknown C are much lower than those presented in the main text.

For clarity of the reported values, *Tables S.2 – S33* provide the data. Note that all conversion, selectivity, and yield data is reported as a fraction, with the absolute error derived from the error propagation analysis given.

Table S.2 | Conversion data (%) for the 10:5 slm, CO_2:CH_4 set.

CO_2:CH_4 slm	Power (W)	Pressure (mbar)	Expansion (α)	CO_2 Conversion (%)		CH_4 Conversion (%)		Total Conversion
				Absolute	Effective	Absolute	Effective	
10:5	1000	200	1.04	28.0 ± 1.4	18.8 ± 0.7	23.5 ± 3.7	7.7 ± 0.9	26.5 ± 1.1
10:5	1000	500	1.04	28.3 ± 1.4	18.9 ± 0.7	23.7 ± 3.7	7.7 ± 0.9	26.8 ± 1.1
10:5	1000	700	1.04	28.2 ± 1.4	18.9 ± 0.7	23.9 ± 3.7	7.8 ± 0.9	26.8 ± 1.1
10:5	1000	900	1.03	28.1 ± 1.4	18.8 ± 0.7	23.9 ± 3.7	7.8 ± 0.9	26.8 ± 1.1
10:5	1250	200	1.05	35.2 ± 1.3	23.6 ± 0.7	32.7 ± 3.6	10.7 ± 0.9	34.4 ± 1.1
10:5	1250	500				No data		
10:5	1250	700	1.05	35.4 ± 1.3	23.7 ± 0.7	32.9 ± 3.6	10.8 ± 0.9	34.6 ± 1.1
10:5	1250	900	1.05	35.6 ± 1.3	23.9 ± 0.7	33.4 ± 3.6	10.9 ± 0.9	34.9 ± 1.1

Table S.3 | Conversion data (%) for the 10:14 slm, CO_2:CH_4 set.

CO_2:CH_4 slm	Power (W)	Pressure (mbar)	Expansion (α)	CO_2 Conversion (%)		CH_4 Conversion (%)		Total Conversion
				Absolute	Effective	Absolute	Effective	
10:14	1000	200	1.02	27.6 ± 1.9	11.7 ± 0.7	8.7 ± 2.4	5.0 ± 1.1	16.7 ± 1.3
10:14	1000	500	1.04	27.5 ± 1.9	11.6 ± 0.7	8.1 ± 2.5	4.7 ± 1.1	16.3 ± 1.3
10:14	1000	700	1.04	28.0 ± 1.9	11.8 ± 0.7	8.3 ± 2.4	4.8 ± 1.1	16.7 ± 1.3
10:14	1000	900	1.03	28.3 ± 1.9	11.9 ± 0.7	8.8 ± 2.4	5.1 ± 1.1	17.0 ± 1.3
10:14	1250	200	0.98	39.1 ± 1.6	16.5 ± 0.6	16.8 ± 2.2	9.7 ± 1.0	26.2 ± 1.2
10:14	1250	500	0.98	39.5 ± 1.6	16.7 ± 0.6	16.5 ± 2.2	9.5 ± 1.0	26.2 ± 1.2
10:14	1250	700	1.04	35.5 ± 1.6	15.0 ± 0.6	12.0 ± 2.2	6.9 ± 1.0	21.9 ± 1.2
10:14	1250	900	1.02	39.6 ± 1.8	15.6 ± 0.7	13.9 ± 2.4	8.0 ± 1.1	23.6 ± 1.3

Table S.4 | Conversion data (%) for the 7:7 slm, CO_2:CH_4 set.

CO_2:CH_4 slm	Power (W)	Pressure (mbar)	Expansion (α)	CO_2 Conversion (%)		CH_4 Conversion (%)		Total Conversion
				Absolute	Effective	Absolute	Effective	
7:7	1000	200	1.06	38.8 ± 1.5	19.6 ± 0.6	19.8 ± 2.6	9.8 ± 0.9	29.4 ± 1.1
7:7	1000	500	1.06	39.5 ± 1.5	20.0 ± 0.6	19.8 ± 2.6	9.8 ± 0.9	29.8 ± 1.1
7:7	1000	700	1.06	39.5 ± 1.5	20.0 ± 0.6	20.0 ± 2.6	9.9 ± 0.9	29.9 ± 1.1
7:7	1000	900	1.06	39.3 ± 1.5	19.9 ± 0.6	19.8 ± 2.6	9.8 ± 0.9	29.6 ± 1.1
7:7	1250	200				No data		
7:7	1250	500	1.02	54.6 ± 1.3	27.6 ± 0.6	36.7 ± 2.3	18.1 ± 0.9	45.8 ± 1.0
7:7	1250	700	1.04	52.1 ± 1.3	26.4 ± 0.6	29.9 ± 2.3	14.8 ± 0.9	41.1 ± 1.0
7:7	1250	900	1.08	49.6 ± 1.4	25.1 ± 0.6	26.6 ± 2.4	13.2 ± 0.9	38.2 ± 1.1

Table S.5 | Conversion data (%) for the 7:14 slm, CO_2:CH_4 set.

CO_2:CH_4 slm	Power (W)	Pressure (mbar)	Expansion (α)	CO_2 Conversion (%)		CH_4 Conversion (%)		Total Conversion
				Absolute	Effective	Absolute	Effective	
7:14	1000	200		No data				
7:14	1000	500	1.03	41.1 ± 1.3	13.9 ± 0.5	10.3 ± 1.6	6.8 ± 0.8	20.7 ± 0.9
7:14	1000	700	1.05	40.3 ± 1.3	13.6 ± 0.5	9.6 ± 1.6	6.3 ± 0.8	20.0 ± 0.9
7:14	1000	900	1.03	40.3 ± 1.3	13.7 ± 0.5	10.3 ± 1.6	6.8 ± 0.8	20.5 ± 0.9
7:14	1250	200	1.07	51.2 ± 1.2	17.3 ± 0.5	14.2 ± 1.5	9.4 ± 0.8	26.7 ± 0.9
7:14	1250	500	1.08	52.3 ± 1.2	17.7 ± 0.5	14.4 ± 1.5	9.5 ± 0.8	27.2 ± 0.9
7:14	1250	700	1.07	52.6 ± 1.2	17.8 ± 0.5	14.6 ± 1.5	9.7 ± 0.8	27.5 ± 0.9
7:14	1250	900	1.07	52.4 ± 1.1	17.7 ± 0.5	14.4 ± 1.5	9.5 ± 0.8	27.3 ± 0.9

Table S.6 | SEI and EC data and H_2/CO ratio for the 10:5 slm, CO_2:CH_4 set.

CO_2:CH_4 slm	Power (W)	Pressure (mbar)	SEI [kJ/mol]	Energy Cost [kJ/mol]	SEI [kJ/L]	Energy Cost [kJ/L]	SEI [eV/molecule]	Energy Cost [eV/molecule]	H_2/CO Ratio
10:5	1000	200	98 ± 5	371 ± 19	4.09 ± 0.20	15.40 ± 0.77	1.02 ± 0.05	3.84 ± 0.19	0.17
10:5	1000	500	98 ± 5	367 ± 18	4.09 ± 0.20	15.27 ± 0.76	1.02 ± 0.05	3.81 ± 0.19	0.16
10:5	1000	700	98 ± 5	367 ± 18	4.09 ± 0.20	15.28 ± 0.76	1.02 ± 0.05	3.81 ± 0.19	0.16
10:5	1000	900	98 ± 5	368 ± 18	4.09 ± 0.20	14.86 ± 0.76	1.02 ± 0.05	3.81 ± 0.19	0.17
10:5	1250	200	123 ± 6	357 ± 18	5.11 ± 0.26	14.57 ± 0.74	1.27 ± 0.06	3.70 ± 0.19	0.21
10:5	1250	500			No data				
10:5	1250	700	123 ± 6	356 ± 18	5.11 ± 0.26	14.78 ± 0.74	1.27 ± 0.06	3.68 ± 0.19	0.20
10:5	1250	900	123 ± 6	352 ± 18	5.11 ± 0.26	14.64 ± 0.73	1.27 ± 0.06	3.65 ± 0.19	0.20

Table S.7 | SEI and EC data and H_2/CO ratio for the 10:14 slm, CO_2:CH_4 set.

CO_2:CH_4 slm	Power (W)	Pressure (mbar)	SEI [kJ/mol]	Energy Cost [kJ/mol]	SEI [kJ/L]	Energy Cost [kJ/L]	SEI [eV/molecule]	Energy Cost [eV/molecule]	H_2/CO Ratio
10:14	1000	200	62 ± 3	371 ± 19	2.57 ± 0.13	15.41 ± 0.77	0.64 ± 0.03	3.84 ± 0.19	0.21
10:14	1000	500	62 ± 3	380 ± 19	2.57 ± 0.13	15.77 ± 0.79	0.64 ± 0.03	3.93 ± 0.20	0.22
10:14	1000	700	62 ± 3	371 ± 19	2.57 ± 0.13	15.43 ± 0.77	0.64 ± 0.03	3.85 ± 0.19	0.22
10:14	1000	900	62 ± 3	364 ± 18	2.57 ± 0.13	15.12 ± 0.76	0.64 ± 0.03	3.77 ± 0.19	0.22
10:14	1250	200	77 ± 4	295 ± 15	3.21 ± 0.16	12.25 ± 0.61	0.80 ± 0.04	3.05 ± 0.15	0.27
10:14	1250	500	77 ± 4	295 ± 15	3.21 ± 0.16	12.26 ± 0.61	0.80 ± 0.04	3.06 ± 0.15	0.26
10:14	1250	700	77 ± 4	353 ± 18	3.21 ± 0.16	14.67 ± 0.73	0.80 ± 0.04	3.66 ± 0.18	0.26
10:14	1250	900	77 ± 4	327 ± 16	3.21 ± 0.16	13.60 ± 0.68	0.80 ± 0.04	3.39 ± 0.17	0.26

Table S.8 | SEI and EC data and H_2/CO ratio for the 7:7 slm, CO_2:CH_4 set.

CO_2:CH_4 slm	Power (W)	Pressure (mbar)	SEI [kJ/mol]	Energy Cost [kJ/mol]	SEI [kJ/L]	Energy Cost [kJ/L]	SEI [eV/molecule]	Energy Cost [eV/molecule]	H_2/CO Ratio
7:7	1000	200	106 ± 5	360 ± 19	4.40 ± 0.22	14.96 ± 0.75	1.10 ± 0.05	3.73 ± 0.19	0.24
7:7	1000	500	106 ± 5	355 ± 18	4.40 ± 0.22	14.76 ± 0.74	1.10 ± 0.05	3.68 ± 0.18	0.23
7:7	1000	700	106 ± 5	354 ± 18	4.40 ± 0.22	14.72 ± 0.74	1.10 ± 0.05	3.67 ± 0.18	0.23
7:7	1000	900	106 ± 5	357 ± 18	4.40 ± 0.22	14.84 ± 0.74	1.10 ± 0.05	3.70 ± 0.18	0.23
7:7	1250	200			No data				
7:7	1250	500	132 ± 7	289 ± 18	5.50 ± 0.27	12.01 ± 0.60	1.37 ± 0.07	3.00 ± 0.15	0.30
7:7	1250	700	132 ± 7	322 ± 18	5.50 ± 0.27	13.37 ± 0.67	1.37 ± 0.07	3.33 ± 0.17	0.29
7:7	1250	900	132 ± 7	346 ± 18	5.50 ± 0.27	14.38 ± 0.72	1.37 ± 0.07	3.59 ± 0.18	0.29

Table S.9 | SEI and EC data and H₂/CO ratio for the 7:14 slm, CO₂:CH₄ set.

CO_2:CH_4 slm	Power (W)	Pressure (mbar)	SEI [kJ/mol]	Energy Cost [kJ/mol]	SEI [kJ/L]	Energy Cost [kJ/L]	SEI [eV/molecule]	Energy Cost [eV/molecule]	H_2/CO Ratio
7:14	1000	200				No data			
7:14	1000	500	71 ± 4	342 ± 17	2.94 ± 0.15	14.23 ± 0.71	0.73 ± 0.04	3.55 ± 0.18	0.29
7:14	1000	700	71 ± 4	355 ± 18	2.57 ± 0.15	14.74 ± 0.74	0.73 ± 0.04	3.68 ± 0.18	0.29
7:14	1000	900	71 ± 4	346 ± 17	2.57 ± 0.15	14.37 ± 0.72	0.73 ± 0.04	3.58 ± 0.18	0.29
7:14	1250	200	89 ± 4	332 ± 17	3.68 ± 0.18	13.78 ± 0.69	0.92 ± 0.05	3.44 ± 0.17	0.37
7:14	1250	500	89 ± 4	325 ± 16	3.68 ± 0.18	13.51 ± 0.68	0.92 ± 0.05	3.37 ± 0.17	0.38
7:14	1250	700	89 ± 4	322 ± 16	3.68 ± 0.18	13.38 ± 0.67	0.92 ± 0.05	3.34 ± 0.17	0.38
7:14	1250	900	89 ± 4	325 ± 16	3.68 ± 0.18	13.49 ± 0.67	0.92 ± 0.05	3.36 ± 0.17	0.37

Table S.10 | Carbon selectivity (%) for the 10:5 slm CO₂:CH₄ set.

Power (W)	Pressure (mbar)	CO	C_2H_4	C_2H_6	C_2H_2	Unknown
1000	200	87.0 ± 6.9	1.8 ± 0.5	1.1 ± 0.3	1.6 ± 0.6	8.5
1000	500	89.0 ± 7.0	1.2 ± 0.5	0.5 ± 0.3	0.7 ± 0.6	8.5
1000	700	89.2 ± 7.0	1.1 ± 0.5	0.4 ± 0.3	0.6 ± 0.6	8.7
1000	900	88.0 ± 6.9	1.0 ± 0.5	0.3 ± 0.3	0.5 ± 0.6	10.1
1250	200	90.7 ± 5.6	1.7 ± 0.4	0.8 ± 0.2	1.2 ± 0.5	5.5
1250	500			No data		
1250	700	91.9 ± 5.6	1.0 ± 0.4	0.3 ± 0.2	0.5 ± 0.5	6.3
1250	900	93.1 ± 5.6	1.0 ± 0.4	0.3 ± 0.2	0.4 ± 0.5	5.3

Table S.11 | Carbon selectivity (%) for the 10:14 slm CO₂:CH₄ set.

Power (W)	Pressure (mbar)	CO	C_2H_4	C_2H_6	C_2H_2	Unknown
1000	200	89.9 ± 4.5	2.4 ± 0.3	1.9 ± 0.2	2.7 ± 0.3	3.1
1000	500	99.0 ± 5.1	2.0 ± 0.3	1.1 ± 0.2	1.6 ± 0.3	-3.7
1000	700	98.8 ± 5.0	1.7 ± 0.3	0.9 ± 0.1	1.2 ± 0.3	-2.5
1000	900	97.8 ± 4.8	1.5 ± 0.3	0.7 ± 0.1	0.9 ± 0.3	-0.9
1250	200	73.5 ± 2.3	1.8 ± 0.2	1.3 ± 0.1	1.8 ± 0.2	21.7
1250	500	76.6 ± 2.4	1.3 ± 0.2	0.7 ± 0.1	1.0 ± 0.2	20.3
1250	700	97.4 ± 3.5	1.5 ± 0.2	0.7 ± 0.1	1.0 ± 0.2	-0.6
1250	900	88.7 ± 3.2	1.2 ± 0.2	0.5 ± 0.1	0.7 ± 0.2	8.8

Table S.12 | Carbon selectivity (%) for the 7:7 slm CO₂:CH₄ set.

Power (W)	Pressure (mbar)	CO	C_2H_4	C_2H_6	C_2H_2	Unknown
1000	200	91.2 ± 2.2	2.4 ± 0.2	1.5 ± 0.1	2.0 ± 0.2	2.9
1000	500	93.4 ± 2.3	1.6 ± 0.2	0.7 ± 0.1	1.0 ± 0.2	3.4
1000	700	94.3 ± 2.3	1.3 ± 0.2	0.5 ± 0.1	0.7 ± 0.2	3.1
1000	900	95.5 ± 2.3	1.2 ± 0.2	0.4 ± 0.1	0.6 ± 0.2	2.3
1250	200			No data		
1250	500	72.5 ± 1.2	1.2 ± 0.1	0.4 ± 0.1	0.6 ± 0.1	25.4
1250	700	85.6 ± 1.5	1.1 ± 0.1	0.3 ± 0.1	0.5 ± 0.1	12.5
1250	900	94.7 ± 1.8	1.1 ± 0.1	0.3 ± 0.1	0.4 ± 0.2	3.6

Table S.13 | Carbon selectivity (%) for the 7:14 slm CO_2:CH_4 set.

Power (W)	Pressure (mbar)	CO	C_2H_4	C_2H_6	C_2H_2	Unknown
1000	200			No data		
1000	500	91.5 ± 3.5	2.0 ± 0.2	1.1 ± 0.1	1.5 ± 0.3	4.0
1000	700	96.6 ± 3.8	1.8 ± 0.2	0.9 ± 0.1	1.2 ± 0.3	-0.4
1000	900	92.6 ± 3.5	1.5 ± 0.2	0.7 ± 0.1	0.9 ± 0.3	4.3
1250	200	92.9 ± 2.8	2.6 ± 0.2	1.5 ± 0.1	2.1 ± 0.2	0.9
1250	500	95.7 ± 2.8	1.9 ± 0.2	0.9 ± 0.1	1.2 ± 0.2	0.4
1250	700	95.4 ± 2.8	1.6 ± 0.2	0.7 ± 0.1	0.9 ± 0.2	1.4
1250	900	96.4 ± 2.8	1.4 ± 0.2	0.5 ± 0.1	0.7 ± 0.2	1.0

Table S.14 | Carbon yield (%) for the 10:5 slm CO_2:CH_4 set.

Power (W)	Pressure (mbar)	CO	C_2H_4	C_2H_6	C_2H_2	Unknown
1000	200	23.1 ± 0.2	0.5 ± 5e-2	0.3 ± 3e-2	0.4 ± 6e-2	2.2
1000	500	23.9 ± 0.2	0.3 ± 5e-2	0.1 ± 3e-2	0.2 ± 6e-2	2.2
1000	700	23.9 ± 0.2	0.3 ± 5e-2	0.1 ± 3e-2	0.2 ± 6e-2	2.3
1000	900	23.6 ± 0.2	0.3 ± 5e-2	0.1 ± 3e-2	0.1 ± 6e-2	2.7
1250	200	31.2 ± 0.3	0.6 ± 5e-2	0.3 ± 3e-2	0.4 ± 6e-2	1.9
1250	500			No data		
1250	700	31.8 ± 0.3	0.4 ± 5e-2	0.1 ± 3e-2	0.2 ± 6e-2	2.2
1250	900	32.5 ± 0.3	0.3 ± 5e-2	0.1 ± 3e-2	0.1 ± 6e-2	1.8

Table S.15 | Carbon yield (%) for the 10:14 slm CO_2:CH_4 set.

Power (W)	Pressure (mbar)	CO	C_2H_4	C_2H_6	C_2H_2	Unknown
1000	200	15.3 ± 0.2	0.4 ± 4e-2	0.3 ± 2e-2	0.5 ± 5e-2	0.2
1000	500	16.5 ± 0.2	0.3 ± 4e-2	0.2 ± 2e-2	0.3 ± 5e-2	-1.0
1000	700	16.8 ± 0.2	0.3 ± 4e-2	0.1 ± 2e-2	0.2 ± 5e-2	-0.8
1000	900	17.0 ± 0.2	0.3 ± 4e-2	0.1 ± 2e-2	0.2 ± 5e-2	-0.5
1250	200	19.6 ± 0.2	0.5 ± 4e-2	0.3 ± 2e-2	0.5 ± 5e-2	5.4
1250	500	20.4 ± 0.2	0.4 ± 4e-2	0.2 ± 2e-2	0.3 ± 5e-2	5.0
1250	700	21.7 ± 0.2	0.3 ± 4e-2	0.2 ± 2e-2	0.2 ± 5e-2	-0.6
1250	900	21.3 ± 0.2	0.3 ± 4e-2	0.1 ± 2e-2	0.2 ± 5e-2	1.7

Table S.16 | Carbon yield (%) for the 7:7 slm CO_2:CH_4 set.

Power (W)	Pressure (mbar)	CO	C_2H_4	C_2H_6	C_2H_2	Unknown
1000	200	27.1 ± 0.2	0.7 ± 5e-2	0.4 ± 3e-2	0.6 ± 6e-2	0.5
1000	500	28.1 ± 0.2	0.5 ± 5e-2	0.2 ± 3e-2	0.3 ± 6e-2	0.7
1000	700	28.5 ± 0.2	0.4 ± 5e-2	0.2 ± 3e-2	0.2 ± 6e-2	0.6
1000	900	28.6 ± 0.2	0.4 ± 5e-2	0.1 ± 3e-2	0.2 ± 6e-2	0.4
1250	200			No data		
1250	500	33.4 ± 0.3	0.5 ± 5e-2	0.2 ± 3e-2	0.3 ± 6e-2	11.4
1250	700	35.5 ± 0.3	0.4 ± 5e-2	0.1 ± 3e-2	0.2 ± 6e-2	4.8
1250	900	36.5 ± 0.3	0.4 ± 5e-2	0.1 ± 3e-2	0.2 ± 6e-2	1.0

Table S.17 | Carbon yield (%) for the 7:14 slm CO_2:CH_4 set.

Power (W)	Pressure (mbar)	CO	C_2H_4	C_2H_6	C_2H_2	Unknown
1000	200			No data		
1000	500	19.4 ± 0.2	$0.4 \pm$ 4e-2	$0.2 \pm$ 2e-2	$0.3 \pm$ 5e-2	0.3
1000	700	19.8 ± 0.2	$0.4 \pm$ 4e-2	$0.2 \pm$ 2e-2	$0.2 \pm$ 5e-2	-0.6
1000	900	19.5 ± 0.2	$0.3 \pm$ 4e-2	$0.1 \pm$ 2e-2	$0.2 \pm$ 5e-2	0.4
1250	200	25.4 ± 0.2	$0.7 \pm$ 4e-2	$0.4 \pm$ 2e-2	$0.6 \pm$ 5e-2	-0.4
1250	500	26.7 ± 0.3	$0.5 \pm$ 4e-2	$0.2 \pm$ 2e-2	$0.3 \pm$ 5e-2	-0.6
1250	700	26.9 ± 0.3	$0.5 \pm$ 4e-2	$0.2 \pm$ 2e-2	$0.3 \pm$ 5e-2	-0.3
1250	900	26.9 ± 0.3	$0.4 \pm$ 4e-2	$0.1 \pm$ 2e-2	$0.2 \pm$ 5e-2	-0.4

Table S.18 | Oxygen selectivity (%) for the 10:5 slm CO_2:CH_4 set.

Power (W)	Pressure (mbar)	CO	O_2	Unknown
1000	200	60.1 ± 3.2	6.8 ± 1.4	33.0
1000	500	61.5 ± 3.2	4.1 ± 0.9	34.3
1000	700	61.9 ± 3.3	3.4 ± 0.7	34.7
1000	900	61.1 ± 3.2	2.8 ± 0.6	36.0
1250	200	64.6 ± 2.4	3.8 ± 0.6	31.7
1250	500		No data	
1250	700	65.4 ± 2.4	1.7 ± 0.3	32.9
1250	900	66.5 ± 2.4	1.4 ± 0.2	32.2

Table S.19 | Oxygen selectivity (%) for the 10:14 slm CO_2:CH_4 set.

Power (W)	Pressure (mbar)	CO	O_2	Unknown
1000	200	62.8 ± 5.6	11.4 ± 3.3	25.8
1000	500	67.9 ± 5.9	8.2 ± 2.4	24.0
1000	700	68.0 ± 5.7	6.7 ± 1.9	25.3
1000	900	68.2 ± 5.6	5.5 ± 1.6	26.4
1250	200	56.7 ± 3.0	5.9 ± 1.2	37.4
1250	500	58.6 ± 3.0	3.9 ± 0.8	37.5
1250	700	69.6 ± 3.9	3.7 ± 0.8	26.7
1250	900	65.6 ± 3.6	2.8 ± 0.6	31.6

Table S.20 | Oxygen selectivity (%) for the 7:7 slm CO_2:CH_4 set.

Power (W)	Pressure (mbar)	CO	O_2	Unknown
1000	200	66.9 ± 3.0	4.6 ± 0.9	28.6
1000	500	68.1 ± 2.9	1.8 ± 0.3	30.1
1000	700	69.0 ± 2.9	1.1 ± 0.2	30.0
1000	900	69.7 ± 3.0	0.8 ± 0.2	29.5
1250	200		No data	
1250	500	58.5 ± 1.6	0.9 ± 0.1	40.6
1250	700	65.2 ± 1.8	$0.3 \pm$ 5e-2	34.4
1250	900	70.6 ± 2.1	$0.2 \pm$ 2e-2	29.3

Table S.21 | Oxygen selectivity (%) for the 7:14 slm CO_2:CH_4 set.

Power (W)	Pressure (mbar)	CO	O_2	Unknown
1000	200		No data	
1000	500	66.4 ± 4.1	4.8 ± 1.2	28.9
1000	700	69.0 ± 4.3	3.6 ± 0.9	27.5
1000	900	67.7 ± 4.3	2.7 ± 0.7	29.6
1250	200	69.7 ± 3.0	3.6 ± 0.7	26.7
1250	500	71.6 ± 3.0	1.6 ± 0.3	26.8
1250	700	71.7 ± 3.0	1.0 ± 0.2	27.4
1250	900	72.1 ± 3.0	0.7 ± 0.1	27.2

Table S.22 | Oxygen yield (%) for the 10:5 slm CO_2:CH_4 set.

Power (W)	Pressure (mbar)	CO	O_2	Unknown
1000	200	16.8 ± 0.1	1.9 ± 0.1	18.9
1000	500	17.4 ± 0.1	1.2 ± 0.1	19.4
1000	700	17.4 ± 0.1	$1.0 \pm 5e\text{-}2$	19.4
1000	900	17.2 ± 0.1	$0.8 \pm 4e\text{-}2$	19.8
1250	200	22.7 ± 0.1	1.3 ± 0.1	23.3
1250	500		No data	
1250	700	23.2 ± 0.1	$0.6 \pm 3e\text{-}2$	23.8
1250	900	23.7 ± 0.1	$0.5 \pm 3e\text{-}2$	23.7

Table S.23 | Oxygen yield (%) for the 10:14 slm CO_2:CH_4 set.

Power (W)	Pressure (mbar)	CO	O_2	Unknown
1000	200	17.4 ± 0.2	3.2 ± 0.2	2.8
1000	500	18.7 ± 0.2	2.3 ± 0.1	2.3
1000	700	19.1 ± 0.2	1.9 ± 0.1	2.7
1000	900	19.3 ± 0.2	1.5 ± 0.1	3.1
1250	200	22.2 ± 0.2	2.3 ± 0.1	8.6
1250	500	23.1 ± 0.2	1.6 ± 0.1	8.7
1250	700	24.7 ± 0.2	1.3 ± 0.1	4.0
1250	900	24.2 ± 0.2	$1.0 \pm 5e\text{-}2$	5.9

Table S.24 | Oxygen yield (%) for the 7:7 slm CO_2:CH_4 set.

Power (W)	Pressure (mbar)	CO	O_2	Unknown
1000	200	25.9 ± 0.2	1.8 ± 0.1	11.5
1000	500	26.9 ± 0.2	$0.7 \pm 4e\text{-}2$	12.4
1000	700	27.3 ± 0.2	$0.4 \pm 2e\text{-}2$	12.3
1000	900	27.4 ± 0.2	$0.3 \pm 2e\text{-}2$	12.0
1250	200		No data	
1250	500	32.0 ± 0.2	$0.5 \pm 3e\text{-}2$	22.8
1250	700	34.0 ± 0.2	$0.2 \pm 1e\text{-}2$	18.6
1250	900	35.0 ± 0.2	$0.1 \pm 4e\text{-}3$	15.1

Table S.25 | Oxygen yield (%) for the 7:14 slm CO_2:CH_4 set.

Power (W)	Pressure (mbar)	CO	O_2	Unknown
1000	200		No data	
1000	500	27.3 ± 0.3	2.0 ± 0.1	-1.4
1000	700	27.8 ± 0.3	1.4 ± 0.1	-1.9
1000	900	27.3 ± 0.3	$1.1 \pm 5e\text{-}2$	-1.1
1250	200	35.7 ± 0.3	1.8 ± 0.1	-2.9
1250	500	37.5 ± 0.3	$0.8 \pm 4e\text{-}2$	-2.9
1250	700	37.7 ± 0.3	$0.5 \pm 3e\text{-}2$	-2.6
1250	900	37.8 ± 0.3	$0.3 \pm 2e\text{-}2$	-2.7

Table S.26 | Hydrogen selectivity (%) for the 10:5 slm CO_2:CH_4 set.

Power (W)	Pressure (mbar)	H_2	C_2H_4	C_2H_6	C_2H_2	Unknown
1000	200	27.4 ± 2.3	3.3 ± 0.4	3.0 ± 0.3	1.4 ± 0.2	64.9
1000	500	25.8 ± 2.2	2.2 ± 0.3	1.4 ± 0.3	0.7 ± 0.2	69.8
1000	700	26.2 ± 2.2	2.0 ± 0.3	1.1 ± 0.3	0.5 ± 0.2	70.2
1000	900	26.2 ± 2.2	1.8 ± 0.3	0.9 ± 0.3	0.4 ± 0.2	70.7
1250	200	31.7 ± 1.7	2.9 ± 0.3	2.1 ± 0.2	1.0 ± 0.1	62.3
1250	500			No data		
1250	700	30.9 ± 1.7	1.7 ± 0.2	0.8 ± 0.2	0.4 ± 0.1	66.1
1250	900	31.5 ± 1.7	1.6 ± 0.2	0.7 ± 0.2	0.3 ± 0.1	65.9

Table S.27 | Hydrogen selectivity (%) for the 10:14 slm CO2:CH4 set.

Power (W)	Pressure (mbar)	H_2	C_2H_4	C_2H_6	C_2H_2	Unknown
1000	200	33.6 ± 4.2	4.2 ± 0.6	5.0 ± 0.6	2.3 ± 0.4	54.9
1000	500	39.8 ± 5.1	3.6 ± 0.6	3.2 ± 0.5	1.5 ± 0.3	51.9
1000	700	40.0 ± 4.9	3.0 ± 0.5	2.3 ± 0.4	1.1 ± 0.3	53.6
1000	900	38.5 ± 4.5	2.6 ± 0.5	1.8 ± 0.4	0.8 ± 0.3	56.3
1250	200	28.1 ± 1.9	2.6 ± 0.2	2.7 ± 0.2	1.3 ± 0.1	65.3
1250	500	28.9 ± 1.9	1.9 ± 0.2	1.6 ± 0.2	0.7 ± 0.1	66.8
1250	700	41.9 ± 3.4	2.5 ± 0.4	1.8 ± 0.3	0.8 ± 0.2	53.0
1250	900	35.4 ± 2.7	1.9 ± 0.3	1.2 ± 0.2	0.6 ± 0.2	60.8

Table S.28 | Hydrogen selectivity (%) for the 7:7 slm CO2:CH4 set.

Power (W)	Pressure (mbar)	H_2	C_2H_4	C_2H_6	C_2H_2	Unknown
1000	200	34.8 ± 2.1	3.7 ± 0.3	3.5 ± 0.3	1.6 ± 0.2	64.9
1000	500	34.1 ± 2.1	2.5 ± 0.3	1.7 ± 0.2	0.8 ± 0.2	69.8
1000	700	34.3 ± 2.1	2.1 ± 0.3	1.2 ± 0.2	0.6 ± 0.2	70.2
1000	900	35.1 ± 2.1	1.9 ± 0.3	1.0 ± 0.2	0.5 ± 0.2	70.7
1250	200			No data		
1250	500	28.7 ± 1.0	1.5 ± 0.1	0.8 ± 0.1	0.4 ± 0.1	66.2
1250	700	35.9 ± 1.4	1.6 ± 0.2	0.7 ± 0.1	0.3 ± 0.1	66.1
1250	900	41.5 ± 1.7	1.6 ± 0.2	0.7 ± 0.2	0.3 ± 0.1	65.9

Table S.29 | Hydrogen selectivity (%) for the 7:14 slm CO2:CH4 set.

Power (W)	Pressure (mbar)	H_2	C_2H_4	C_2H_6	C_2H_2	Unknown
1000	200			No data		
1000	500	42.2 ± 3.7	3.2 ± 0.4	2.6 ± 0.3	1.2 ± 0.2	50.9
1000	700	46.5 ± 4.3	3.0 ± 0.4	2.1 ± 0.3	1.0 ± 0.2	47.4
1000	900	41.9 ± 3.7	2.4 ± 0.4	1.5 ± 0.3	0.7 ± 0.2	53.5
1250	200	52.2 ± 3.2	4.0 ± 0.3	3.4 ± 0.3	1.6 ± 0.2	39.0
1250	500	54.2 ± 3.3	2.9 ± 0.3	1.9 ± 0.2	0.9 ± 0.2	40.1
1250	700	53.5 ± 3.2	2.5 ± 0.3	1.5 ± 0.2	0.7 ± 0.1	41.9
1250	900	54.1 ± 3.3	2.1 ± 0.3	1.2 ± 0.2	0.5 ± 0.1	42.1

Table S.30 | Hydrogen yield (%) for the 10:5 slm CO2:CH4 set.

Power (W)	Pressure (mbar)	H_2	C_2H_4	C_2H_6	C_2H_2	Unknown
1000	200	6.4 ± 0.5	0.8 ± 0.1	0.7 ± 0.1	0.3 ± 0.1	22.6
1000	500	6.1 ± 0.5	0.5 ± 0.1	0.3 ± 0.1	0.2 ± 0.1	24.0
1000	700	6.3 ± 0.5	0.5 ± 0.1	0.3 ± 0.1	0.1 ± 0.1	24.3
1000	900	6.3 ± 0.5	0.4 ± 0.1	0.2 ± 0.1	0.1 ± 0.1	24.4
1250	200	10.4 ± 0.5	0.9 ± 0.1	0.7 ± 0.1	0.3 ± 0.1	30.6
1250	500			No data		
1250	700	10.2 ± 0.5	0.6 ± 0.1	0.3 ± 0.1	0.1 ± 0.1	32.1
1250	900	10.5 ± 0.5	0.5 ± 0.1	0.2 ± 0.1	0.1 ± 0.1	32.5

Table S.31 | Hydrogen yield (%) for the 10:14 slm CO2:CH4 set.

Power (W)	Pressure (mbar)	H_2	C_2H_4	C_2H_6	C_2H_2	Unknown
1000	200	2.9 ± 0.2	$0.4 \pm 4e\text{-}2$	$0.4 \pm 3e\text{-}2$	$0.2 \pm 2e\text{-}2$	16.1
1000	500	3.2 ± 0.2	$0.3 \pm 4e\text{-}2$	$0.3 \pm 3e\text{-}2$	$0.1 \pm 2e\text{-}2$	14.8
1000	700	3.3 ± 0.2	$0.3 \pm 4e\text{-}2$	$0.2 \pm 3e\text{-}2$	$0.1 \pm 2e\text{-}2$	15.4
1000	900	3.4 ± 0.2	$0.2 \pm 4e\text{-}2$	$0.2 \pm 3e\text{-}2$	$0.1 \pm 2e\text{-}2$	16.4
1250	200	4.7 ± 0.2	$0.4 \pm 3e\text{-}2$	$0.5 \pm 3e\text{-}2$	$0.2 \pm 2e\text{-}2$	32.9
1250	500	4.8 ± 0.2	$0.3 \pm 3e\text{-}2$	$0.3 \pm 3e\text{-}2$	$0.1 \pm 2e\text{-}2$	32.6
1250	700	5.0 ± 0.2	$0.3 \pm 4e\text{-}2$	$0.2 \pm 3e\text{-}2$	$0.1 \pm 2e\text{-}2$	22.1
1250	900	4.9 ± 0.2	$0.3 \pm 4e\text{-}2$	$0.2 \pm 3e\text{-}2$	$0.1 \pm 2e\text{-}2$	26.7

Table S.32 | Hydrogen yield (%) for the 7:7 slm CO2:CH4 set.

Power (W)	Pressure (mbar)	H_2	C_2H_4	C_2H_6	C_2H_2	Unknown
1000	200	6.9 ± 0.3	$0.7 \pm 5e\text{-}2$	$0.7 \pm 4e\text{-}2$	$0.3 \pm 3e\text{-}2$	30.5
1000	500	6.8 ± 0.3	$0.5 \pm 5e\text{-}2$	$0.3 \pm 4e\text{-}2$	$0.2 \pm 3e\text{-}2$	31.5
1000	700	6.9 ± 0.3	$0.4 \pm 5e\text{-}2$	$0.2 \pm 4e\text{-}2$	$0.1 \pm 3e\text{-}2$	31.9
1000	900	6.9 ± 0.3	$0.4 \pm 5e\text{-}2$	$0.2 \pm 4e\text{-}2$	$0.1 \pm 3e\text{-}2$	31.5
1250	200			No data		
1250	500	10.5 ± 0.3	$0.6 \pm 5e\text{-}2$	$0.3 \pm 4e\text{-}2$	$0.1 \pm 3e\text{-}2$	61.0
1250	700	10.7 ± 0.3	$0.5 \pm 5e\text{-}2$	$0.2 \pm 4e\text{-}2$	$0.1 \pm 3e\text{-}2$	47.5
1250	900	11.0 ± 0.3	$0.4 \pm 5e\text{-}2$	$0.2 \pm 4e\text{-}2$	$0.1 \pm 3e\text{-}2$	40.9

Table S.33 | Hydrogen yield (%) for the 7:14 slm CO2:CH4 set.

Power (W)	Pressure (mbar)	H_2	C_2H_4	C_2H_6	C_2H_2	Unknown
1000	200			No data		
1000	500	4.3 ± 0.2	$0.3 \pm 3e\text{-}2$	$0.3 \pm 3e\text{-}2$	$0.1 \pm 2e\text{-}2$	22.1
1000	700	4.4 ± 0.2	$0.3 \pm 3e\text{-}2$	$0.2 \pm 3e\text{-}2$	$0.1 \pm 2e\text{-}2$	20.2
1000	900	4.3 ± 0.2	$0.2 \pm 3e\text{-}2$	$0.2 \pm 3e\text{-}2$	$0.1 \pm 2e\text{-}2$	22.5
1250	200	7.4 ± 0.2	$0.6 \pm 3e\text{-}2$	$0.5 \pm 3e\text{-}2$	$0.2 \pm 2e\text{-}2$	28.8
1250	500	7.8 ± 0.2	$0.4 \pm 3e\text{-}2$	$0.3 \pm 3e\text{-}2$	$0.1 \pm 2e\text{-}2$	29.5
1250	700	7.8 ± 0.2	$0.4 \pm 3e\text{-}2$	$0.2 \pm 3e\text{-}2$	$0.1 \pm 2e\text{-}2$	30.2
1250	900	7.8 ± 0.2	$0.3 \pm 3e\text{-}2$	$0.2 \pm 3e\text{-}2$	$0.1 \pm 2e\text{-}2$	29.8

S.3.2 Carbon Analysis

During TEM analyses, the particles analyzed were amorphous, as shown and discussed in the main text, except for one group of particles, shown in *Figure S.6* below.
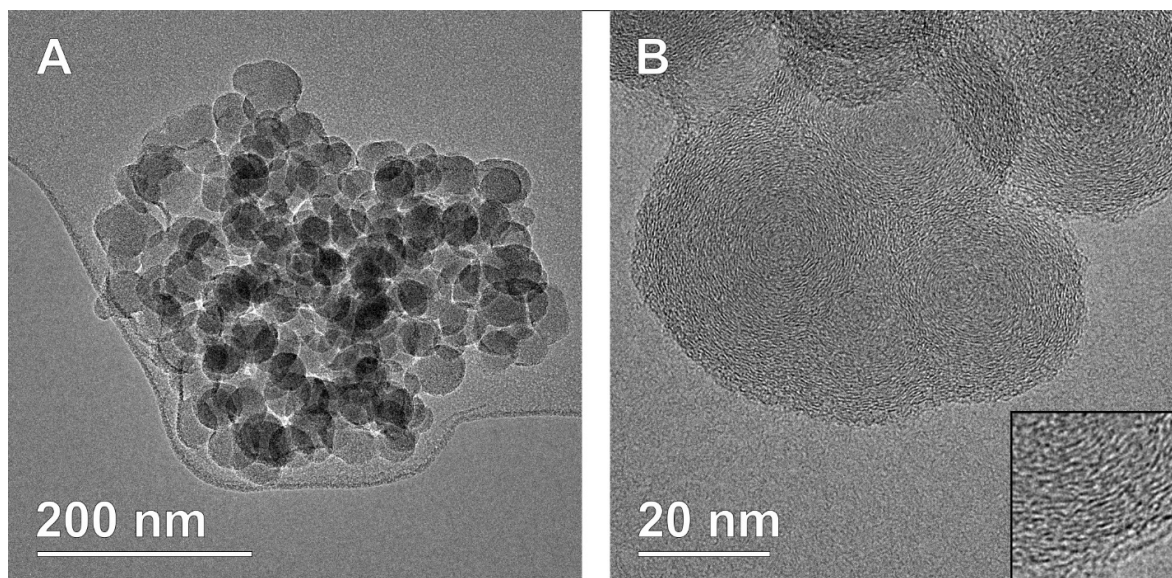

Figure S.6 | A: Group of particles that exhibit a nano-onion-like structure. B: Higher magnification image of one of the nano-onion particles, presenting the indicative layered structure, highlighted in the inset at double the magnification

These particles exhibited a nano-onion type structure, containing some low-range ordering in the form of concentric layers of carbon, in contrast with the completely amorphous particles observed mostly [11]. These particles were rare and are therefore not considered a significant part of the produced materials. Still, it does illustrate that the formation of carbon in this system is not trivial and that there may be inhomogeneities in how different gas fractions are treated.

References

[1] S. Kelly, E. Mercer, R. De Meyer, R.-G. Ciocarlan, S. Bals, A. Bogaerts, Microwave plasma-based dry reforming of methane: Reaction performance and carbon formation, Journal of CO2 Utilization 75 (2023) 102564.

https://doi.org/https://doi.org/10.1016/j.jcou.2023.102564.

[2] E. Carbone, F. D'Isa, A. Hecimovic, U. Fantz, Analysis of the C2 (d3Πg-a3Πu) Swan bands as a thermometric probe in CO2 microwave plasmas, Plasma Sources Science and Technology (2019). https://doi.org/10.1088/1361-6595/ab74b4.

[3] A.J. Wolf, T.W. Righart, F. Peeters, W. Bongers, M. Van De Sanden, Implications of thermo-chemical instability on the contracted modes in CO2 microwave plasmas, Plasma Sources Science and Technology 29(2) (2020) 025005.

https://doi.org/http://dx.doi.org/10.1088/1361-6595/ab5eca.

[4] E.R. Mercer, S. Van Alphen, C.F.A.M. van Deursen, T.W.H. Righart, W.A. Bongers, R. Snyders, A. Bogaerts, M.C.M. van de Sanden, F.J.J. Peeters, Post-plasma Quenching to Improve Conversion and Energy Efficiency in a CO_2 Microwave Plasma, Fuel 334 (2023) 126734. https://doi.org/10.1016/j.fuel.2022.126734.

[5] C. van Deursen, H. Van Poyer, W. Bongers, F. Peeters, F. Smits, M. van de Sanden, Effluent Nozzles in Reverse-Vortex-Stabilized Microwave CO_2 Plasmas for Improved Energy Efficiency, Journal of CO2 Utilization 88 (2024) 102952.

https://doi.org/10.1016/j.jcou.2024.102952.

[6] L. Kuijpers, Influence of methane addition to vortex stabilised CO2 microwave discharges, Applied Physics and Science Education, Eindhoven University of Technology (TU/e), 2023.

[7] J.N. Miller, J.C. Miller, Statistics and chemometrics for analytical chemistry, Signal 100 (1998) 95.

[8] B. Wanten, R. Vertongen, R. De Meyer, A. Bogaerts, Plasma-based CO2 conversion: How to correctly analyze the performance?, Journal of energy chemistry (2023).

[9] D.M.G. Gregory P. Smith, Michael Frenklach, Nigel W. Moriarty, Boris Eiteneer, Mikhail Goldenberg, C. Thomas Bowman, Ronald K. Hanson, Soonho Song, William C. Gardiner, Jr., Vitali V. Lissianski, and Zhiwei Qin, GRI-Mech 3.0.

[10] M. Albrechts, I. Tsonev, A. Bogaerts, Can post-plasma CH4 injection improve plasma-based dry reforming of methane? A modeling study, Green Chemistry 26(18) (2024) 9712-9728. https://doi.org/10.1039/D4GC02889A.

[11] P. Serp, B. Machado, Nanostructured Carbon Materials for Catalysis, The Royal Society of Chemistry2015. https://doi.org/10.1039/9781782622567.